Charge and spin dynamics in a two-dimensional electron gas

A Pugžlys[1,3]**, P J Rizo**[1]**, K Ivanin**[1]**, A Slachter**[1]**, D Reuter**[2]**, A D Wieck**[2]**,
C H van der Wal**[1] **and P H M van Loosdrecht**[1]

[1] Zernike Institute for Advanced Materials, University of Groningen, Nijenborgh 4, 9747 AG
Groningen, The Netherlands
[2] Angewandte Festkörperphysik, Ruhr-Universität Bochum, D-44780 Bochum, Germany

E-mail: p.h.m.van.loosdrecht@rug.nl

Abstract
A number of time-resolved optical experiments probing and controlling the
spin and charge dynamics of the high-mobility two-dimensional electron gas
in a GaAs/AlGaAs heterojunction are discussed. These include time-resolved
reflectivity, luminescence, transient grating, magneto-optical Kerr effect, and
electro-optical Kerr effect experiments. The optical experiments provide
information on the carrier lifetimes and spin dephasing times, as well as
on the carrier diffusion coefficient which directly gives the charge mobility.
A combination of the two types of Kerr experiment proves to be useful in
extracting both the carrier lifetimes and spin dephasing times in a single
experiment.

1. Introduction

Realization of the dream of spintronics [1, 2] requires not only detailed knowledge on how
to inject electron spin currents into functional devices [3], but also profound understanding
of how the spin information eventually gets lost, how it is connected to the charge degree of
freedom, and how to manipulate and control the spin degree of freedom. Some useful spin-
based devices are available, but the final grail of fully spin-based electronics has still not been
reached, despite tremendous progress in the field [2]. Electronic and optical methods are the
two favourite manners to study and manipulate the spin degree of freedom in bulk and confined
semiconductors. In particular, optical methods are quite powerful, since they can address *and*
manipulate the charge and spin degrees of freedom independently. Quite early on it was shown
using transient Faraday spectroscopy that the lifetime of a coherent spin population in n-doped
bulk GaAs can be tremendously long, exceeding 100 ns [4]. Moreover, it has been shown that

---

[3] Present address: Photonics Institute, Vienna University of Technology, Gusshausstrasse 27/387, 1040 Vienna,
Austria.

such a coherent spin population can be transported over tens of micrometres before eventually the coherence is lost [5, 6]. Even though these bulk results are instrumental in the study of spin coherence and control, it is clear, in the light of functional devices, that the properties of confined structures as found in quantum well systems, heterojunctions, and quantum wires and dots are even more important [7–9]. Again, optical methods provide excellent tools to study the charge and spin dynamics of these confined structures. The charge channel can for instance be studied using time-resolved luminescence, reflectivity, and transient grating techniques. The spin degrees of freedom can be addressed using time-resolved magneto-optical Kerr effect, Faraday, and transient spin grating techniques. Finally, using a combination of magneto-optical and electro-optical methods, one can even address both the charge and spin degrees of freedom simultaneously.

This paper presents and compares results from some of these optical techniques as applied to a high-mobility two-dimensional electron gas in a GaAs/AlGaAs heterojunction (HJ2DEG). The different techniques were applied with the same laser system and sample material, allowing a qualitative and quantitative comparison of the results from the different techniques. Moreover, parts of the experiments have been performed under identical conditions on both the 2DEG material and bulk GaAs material. This demonstrates how the techniques are useful for studies on 2DEG systems, and provides evidence that the signals are from the 2DEG system rather than from the surrounding bulk material. Developing a consistent picture of the coupled spin and charge dynamics in the GaAs/AlGaAs multilayer system using only one method is very challenging. Therefore it is better to use results from different methods to collect evidence for the mechanisms that underlie this spin and charge dynamics.

The advantage of using heterojunctions for charge transport is obviously their high carrier mobility, which can be tens of millions of cm^2 V^{-1} s^{-1} at low temperatures. For spin transport, this advantage turns out to be a disadvantage. The long mean free path results in a dephasing of a macroscopic coherent spin state through the coupling to the anisotropic crystal field, leading to dephasing times of the order of a nanosecond or less. Note, however, that optical measurements on heterojunction 2DEGs are challenging because the 2DEG has transition energies in the same spectral region as the underlying buffer layer. This makes optical studies in HJ2DEGs more involved than those on double-sided quantum wells (QWs), which can have transition energies that differ substantially from all other characteristic transitions in the QW structure. As a result, it is for QWs relatively easy to spectrally discern the optical response originating from the QW. For heterojunction 2DEGs, however, one has to disentangle the bulk and 2DEG contributions from the mixed 2DEG/bulk optical response, and this will therefore be discussed for several of the optical techniques used in the experiments.

After an introduction of the samples and the experimental set-up in section 2, the charge and spin dynamics of the HJ2DEG will be discussed in sections 3 and 4, respectively. Next, in section 5, the electro-optical Kerr effect in the presence of an external magnetic field (the MEOKE technique) applied to HJ2DEGs will be discussed. This technique allows for the simultaneous study of both the charge and spin dynamics. Finally, section 6 will summarize and conclude this paper.

2. Sample material and experimental set-up

2.1. GaAs/AlGaAs heterojunction sample

Investigations of the intriguing properties of two-dimensional electron gases (2DEGs) such as the integer and fractional quantum Hall effect have stimulated extensive optical studies of modulation-doped single heterojunctions (see [10] and references therein). These
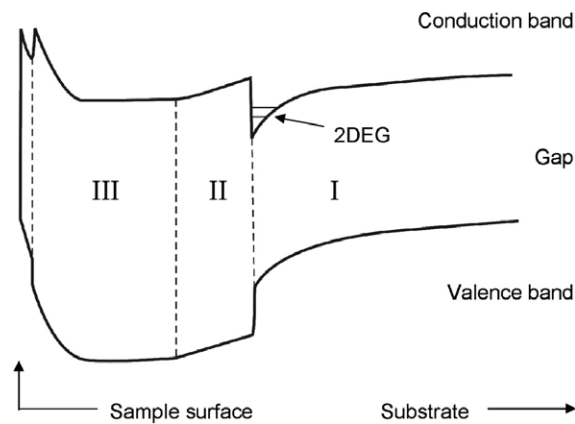
Figure 1. Schematic diagram of the conduction and valence bands along the growth direction (here from right to left) of a heterostructure containing a heterojunction 2DEG. The roman numerals I, II, and III indicate the buffer, spacer, and dopant layers, respectively. The illustration also shows the capping layer above the dopant layer. The 2DEG is localized at the notch potential between the buffer and spacer layers. Notice that a built-in electric field is established across the buffer layer.

heterojunctions show remarkably high carrier mobilities due to the separation of the free carriers from the parent ionized donors and the ability to grow AlGaAs on top of GaAs with extremely low interface roughness [11]. Heterojunction 2DEGs are formed by growing an undoped narrow band gap semiconductor, known as the buffer (or active) layer, in contact with a doped wide band gap semiconductor (or dopant) layer. An undoped spacer layer made of the wide band gap material deposited between the dopant and buffer layers enhances carrier mobility by reducing Coulomb scattering between free carriers and ionized donors. Excess carriers from the dopant layer reduce their energy by a transfer to the conduction band of the narrow band gap semiconductor. Here, these free carriers accumulate at the heterointerface due to electrostatic attraction from the parent ionized donors in the dopant layer, thus forming a 2DEG (see figure 1). The resulting charge separation establishes an electric field or band bending along the growth direction in the buffer layer. The preferred materials for high-mobility 2DEGs are GaAs (buffer layer) and an $Al_x Ga_{1-x} As$ alloy (dopant and spacer layers). The reasons for utilizing these materials are the matching lattice constants, the good interface quality, and the low effective electron mass in the conduction band of GaAs. Note that the term heterojunction will be used for the GaAs/AlGaAs interface where the 2DEG is confined, while the term heterostructure will be used for the entire GaAs/AlGaAs multilayer system.

The experiments described in this paper were performed on a modulation-doped single heterojunction with a band structure as depicted in figure 1. The heterostructure consists of a 9330 Å undoped GaAs buffer layer grown on top of a (100) i-GaAs substrate. On top of this, 368 Å of undoped $Al_{0.32}Ga_{0.68}As$ forms the spacer layer. The dopant layer consists of 719 Å of Si-doped $Al_{0.32}Ga_{0.68}As$ with 3×10^{18} dopants/cm^3. The heterostructure is capped with 55 Å of n-GaAs. The dark mobility and 2DEG carrier density, as derived from transport experiments at 4.2 K, are 1.59×10^6 cm^2 V^{-1} s^{-1} and 2.14×10^{11} cm^{-2}, respectively. After illumination these values become 2.7×10^6 cm^2 V^{-1} s^{-1} and 4.2×10^{11} cm^{-2}.

2.2. Laser system and optical cryostat

In the experiments a cavity dumped titanium sapphire laser (Cascade, Kapteyn-Murnane Laboratories Inc.) was used as a source of excitation and probe light. The laser generates

25 fs, 40 nJ pulses centred around 780 nm. The repetition rate of the laser pulses can be tuned between 40 kHz and 4 MHz. Experiments were performed either by exciting and probing the sample with a broad spectrum corresponding to a 25 fs pulse or with spectral portions having width of ∼10 nm (90% transmission), which were selected using interference filters at appropriate places in the optical set-up. In the latter case, the temporal resolution was about 120 fs. The typical focal spot size in the experiments was about ∼75 μm in diameter, unless stated differently. The energy of the excitation pulses was varied between 100 pJ and 1.2 nJ. Experiments were carried out at temperatures ranging from room temperature down to 4.2 K. In the case of low-temperature measurements the sample was placed in a optical cryostat with a split-pair superconducting magnet system (Spectromag, Oxford Instruments), which allows one to vary the sample temperature from 2 K up to 300 K and is capable of creating an external magnetic field up to 8 T.

3. Charge dynamics

3.1. Photoluminescence

Photoluminescence (PL) studies are very well suited for identifying charge relaxation and recombination mechanisms and their timescales. However, it is well known that PL signals from HJ2DEG samples are dominated by signals from the underlying bulk regions, and it is very difficult to extract the weak signals that are due the 2DEG system. Time-resolved and spectrally resolved PL studies on an HJ2DEG sample, mounted in a cold-finger cryostat, have been performed using streak-camera detection. The results (no data presented here) indeed show strong PL signals that must be attributed to processes in the bulk substrate, and only a very weak signal from the HJ2DEG at high pump intensities. Luminescence from the bulk GaAs buffer layer can be affected by the presence of the 2DEG and the built-in electric field in the buffer layer [12]. Time-resolved PL measurements in the 2DEG sample revealed several PL lines from the GaAs buffer layer. The lifetime of the brightest PL line, the bound exciton line, is strongly dependent on temperature and showed a very slow growth at early times. At 4.2 K after illumination with 780 nm, 120 fs pulses the PL intensity reaches a maximum after 2.3 ns. The PL lifetime measured was 2.35 ns. At 40 K, the peak intensity delay and PL lifetime becomes 0.9 and 9 ns, respectively. For comparison, an i-GaAs sample was measured under identical excitation conditions and the parameters of the bound exciton line were extracted. In this case the peak intensity delay and PL lifetime at 4.2 K were 0.3 and 0.36 ns respectively. At 40 K the decay time remained unchanged within experimental accuracy. Further, the results are consistent with published results from earlier work (discussed below). Since this type of result will be of interest for the discussion of the results from other methods, a summary of the main findings reported in literature will be given here. Note, however, that while many results have been published on this topic, the exact process responsible for the PL associated with 2D electrons in samples with an undoped buffer layer still remains unclear.

In HJ2DEGs the carrier accumulation at the heterointerface bends the buffer layer conduction band below the Fermi level in the region close to the heterojunction [11], as depicted in figure 1. The built-in electric field in the buffer layer rapidly segregates photoexcited electrons toward the heterointerface and holes toward the back of the buffer layer. 2D electron and 3D hole recombination in these heterostructures is then an indirect process in real space. Spatially indirect recombination coupled with the space charge potential present in the buffer layer gives rise to a red shift in the PL energy akin to the quantum-confined Stark effect [13]. In view of the rapid segregation of electrons and holes in heterojunction 2DEGs it is surprising that any holes are present at the heterointerface to recombine with 2D electrons. Significant efforts

have been made to explain the presence of holes near the heterojunction, but the mechanism by which segregated electrons and holes recombine in a heterojunction 2DEG still remains controversial.

Early PL studies identified bands particular to heterojunction structures with a 2DEG and described their features. Yuan *et al* studied the PL from heterojunctions with different layer thickness and Al composition in the barriers [14]. They observed a PL band associated with the heterojunction which they called the H-band, with peak energies between ∼1.505 and ∼1.525 eV (at 1.4 K), depending on excitation density and the Al composition of the barriers. The shift of the PL peak energy with excitation density is a trait intimately linked to the shape of the potential well in heterojunctions. Several other authors have reported a similar PL peak energy shift with excitation density (see for example [15] and [16]). In heterojunction 2DEGs, segregated photoexcited carriers screen the built-in electric field thus flattening the buffer layer bands. 2D electron–3D hole recombination is still indirect in real space but a reduction of the built-in electric field reduces the red shift (produces a blue shift) of the luminescence band. Higher excitation densities generate more photoexcited electrons and holes that segregate and oppose the built-in electric field, thereby increasing the H-band's peak energy. Band gap renormalization due to the high concentration of free carriers at the heterojunction also contributes to the observed spectral shifts.

A blue shift in the H-band PL is also observed when the built-in electric field in the buffer layer is lowered by applying an external bias via a top gate [15]. Reversing the gate bias produces a red shift of the H-band by increasing the band bending [17]. Other PL bands, originating from the buffer layer, show no spectral shifts under intense illumination nor under the influence of an external electric field [14, 16, 18]. The presence of PL lines characteristic of the bulk buffer material highlights the fact that in heterojunction structures 2D carriers are in close relation with bulk carriers. In fact a flat band region can exist in the buffer layer away from the heterojunction which is actually a layer of bulk material. The existence of this flat band region depends on temperature, 2DEG carrier density, buffer layer thickness and unintentional acceptor doping level.

In view of the inevitable interaction of the excitation beam with the buffer layer it is necessary to establish that the H-band is indeed due to recombination involving 2D electrons. This was conclusively demonstrated by Kukushkin *et al* [19] through the modifications of the H-band of a 2DEG in the quantum Hall regime. In their work the authors showed that the PL intensity at the Fermi energy exhibited the same Shubnikov–de Haas oscillations as detected by magneto-transport measurements. By tilting the magnetic field direction, they determined that the observed oscillations depended only on the component of the magnetic field normal to the plane of the heterojunction, a proof of the 2D character of the carriers involved in the PL. Later, Turberfield *et al* [20] and Buhmann *et al* [21] observed the quantum Hall effect at integer and fractional filling factors by modifications to the detected PL from 2D electrons in a heterojunction.

The 2D carrier concentration in the heterojunction can be altered by illumination. A persistent increase in 2DEG density (persistent photoconductivity (PPC)) was observed by Störmer *et al* [11] after illuminating the sample with photons of energy below the AlGaAs band gap. The additional electrons are photoexcited from deep traps called *DX* centres in the AlGaAs. Some of the electrons released tunnel into the GaAs and accumulate in the heterojunction potential well. Chaves *et al* [22] and Chou *et al* [23] observed negative persistent photoconductivity (NPPC) in 2D electron and hole gases in modulation-doped quantum wells, respectively. In this case, illumination with photons above the AlGaAs band gap is necessary. Photoexcited holes in the AlGaAs are swept into the GaAs by the built-in electric field in the spacer layer without having to cross an energy barrier (see figure 1). The holes are then

trapped in the GaAs close to the heterojunction and recombine with 2D electrons, thus reducing the 2DEG density. NPPC and the magneto-optical experiments discussed above demonstrate that 2D electrons can recombine with photoexcited holes even though both carrier types are segregated by the built-in potential in the buffer layer.

Time-resolved PL studies have yielded additional information about photoexcited carrier dynamics in single heterojunctions. After short-pulse excitation, photoexcited carriers drift in opposite directions driven by the built-in electric field. A photoexcited hole with mobility $\mu_h \sim 10^4$ cm V^{-1} s^{-1} in a moderately low built-in electric field E_B of 10^3 V cm^{-1} will drift a distance d of 1 μm away from the heterojunction in roughly $d/\mu_h E_B = 10$ ps. Time-resolved PL measurements can observe the dynamics after the segregated charges have equilibrated. Bergman *et al* [24] measured the time dependence of the H-band PL peak energy. The authors reported a red shift of the H-band peak energy as a function of time. This should be compared to the continuous-wave measurements as a function of excitation density. Reducing the excitation density in this case shifts the H-band PL to lower peak energies [14–16]. In the time-resolved measurements the observed red shift of the H-band peak energy with time is produced by the recovery of the space charge as the photoexcited carriers recombine. Bergman *et al* also measured an increase in the H-band decay time for increasing photon energy, and interpreted it as coming from electrons and holes with larger and larger separations in real space. Electrons and holes in close proximity have large wavefunction overlap, which gives short recombination lifetimes and larger photon energies. Widely separated electrons and holes exhibit longer recombination lifetimes and emit lower-energy photons.

3.2. Transient reflectivity

Transient reflectivity provides important information about carrier dynamics in heterostructures. However, as with photoluminescence studies, the interpretation of the results is not straightforward because of the interaction of pump and probe beams with both the bulk buffer layer and with the 2DEG, and because of the high spectral sensitivity of the reflectivity in the vicinity of the band gap and the 2DEG energy levels. Since the luminescence experiments show that electron–hole segregation occurs in the first few picoseconds, the reflectivity changes observed on a timescale of hundreds of picoseconds to nanoseconds should correspond to the dynamics of the photoinduced carriers in an already equilibrated, segregated charge distribution.

Transient reflectivity changes induced in the heterojunction structure by the pump pulse as a function of probe delay and pump pulse energy at 4.2 K are shown in figure 2. The highest excitation energy trace shows that the ΔR has an initial slow decrease, reaching a negative minimum at a delay of approximately 100 ps. Reducing the pump pulse energy shifts this minimum to later delays.

Several mechanisms could be responsible for the observed delayed formation of the ΔR. A delayed formation similar to that observed in figure 2 has been discussed by Prabhu *et al* [25] for i-GaAs. They showed that a delayed formation could arise at higher temperature and high excitation density from a combination of electron cooling, band filling and band gap renormalization. One could imagine that also in the present case this happens for the 2DEG and the underlying bulk GaAs, leading to the observed delayed formation. The electron energy-loss, or electron cooling, in i-GaAs occurs on a timescale of tens to a hundred ps [26]. The slow formation resulting from this should, however, speed up as the pump pulse energy decreases [27]. This is in contrast to the observation in the HJ2DEG sample, where the minimum of ΔR is reached at later delays when the pump pulse energy is reduced. Alternatively, carrier accumulation in the 2DEG by electron and hole segregation in the built-in electric field of the buffer layer could be responsible for the slow formation of ΔR. Again
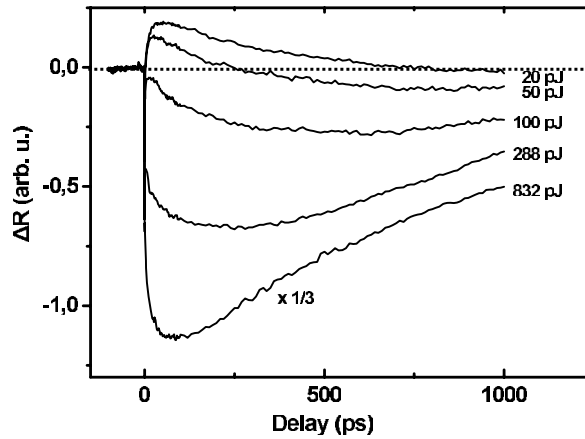
Figure 2. Transient reflectivity (ΔR) traces on the 2DEG sample at different energies per pump pulse. A slow decrease of the signal in the delay range 0 to 100 ps is seen at the highest pump power. As the pulse energy is reduced, the minimum of the signal is reached at later times and the signal becomes positive at early delays. The origin of this signal increase is discussed in the main text. Data taken at 4.2 K, no magnetic field, 780 nm pump, and weaker 820 nm probe pulses.

this process should slow down at higher excitation densities. As discussed in the section on photoluminescence (section 3.1), the segregated carriers in the buffer layer oppose the built-in electric field and reduce it. At a low pump pulse energy the carriers are efficiently separated by the electric field, while at higher pump pulse energy the partial screening produced by the initial segregated carriers reduces the built-in field, thereby slowing down the segregation of the remaining carriers.

Even though the above-discussed phenomena should play a role, they do not explain the observed power dependence of the transient reflectivity response. Time-resolved Kerr rotation experiments (see section 4.1) hint towards a different interpretation. These experiments show the presence of at least two different photoinduced charge populations, each with their own g-factor. Therefore the origin of the slow formation observed in the heterojunction structure studied might very well be related to the detection of carrier dynamics of two different populations, where the observed g-factors suggest that they are of 2D and 3D origin. Both of these carrier populations then independently produce transient reflectivity signals that decay exponentially. In order to explain the observed transient response one of these populations should give a positive ΔR, while the other should give a negative ΔR. Given the complex behaviour of the dielectric function in the vicinity of the band gap and 2DEG level energies, this is not unexpected.

Based on these notions, the sum of two mono-exponential decays of opposite sign has been fitted to the data of figure 2 giving excellent agreement. The difference between the traces at different pump pulse energies is due to changes in the relative amplitude and decay times of the individual signals. The two traces taken at the lowest pump pulse energy show a positive ΔR at early delays that later turns into a negative ΔR. The reason for this is that the lifetime of the population giving negative ΔR is shorter than that of the other population, but its amplitude is larger. Thus, at early delays this population dominates the signal. At later delays, on the other hand, the signal is dominated by the population with the longest lifetime. The estimated carrier lifetimes from fits to the data using the sum of two exponentials with amplitudes of opposite sign are 1200 and 730 ps for the negative and positive contributions, respectively.
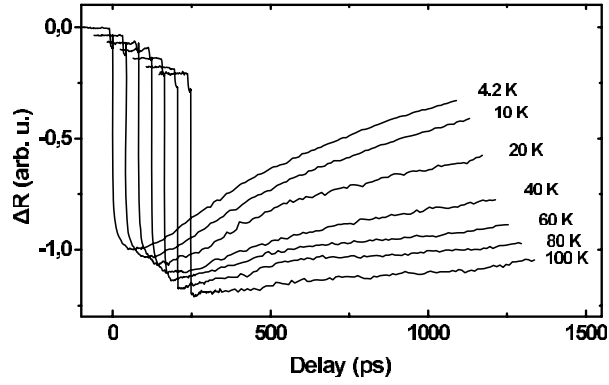
Figure 3. Transient reflectivity of the 2DEG sample as a function of temperature. The lifetime of carriers giving a negative ΔR increases with temperature in a manner comparable with confined carriers [28]. Data taken with pump at 780 nm wavelength and pulse energy of 0.8 nJ and weaker probe at 820 nm, no magnetic field. Data offset for clarity.

Temperature-dependent transient reflectivity measurements, figure 3, shed some light on the origin of the two contributions. The observed increase of the longer lifetime as a function of temperature is consistent with measurements by other groups [28] of carrier recombination time constants in QWs at low temperatures. This suggests that the negative ΔR in figure 2 originates from photoinduced 2D electrons at the heterojunction. The positive ΔR is then produced by 3D carriers, for instance, in the bulk region of the buffer layer.

3.3. Transient grating techniques, probing diffusion and carrier relaxation

One of the disadvantages of time-resolved reflectivity is that for long lifetimes diffusion of carriers out of the laser spot might play an important role. A better, though somewhat more involved, technique to study the carrier (and spin [29, 30]) dynamics is the so-called transient grating technique. The formation of transient gratings (TGs) is a result of a four-wave mixing process which is described by the third-order nonlinear susceptibility $\chi_{ijkl}^{(3)}$. In general $\chi_{ijkl}^{(3)}$ is a fourth-rank tensor with 81 elements. In isotropic media, however, only three elements are independent: $\chi_{xxyy}^{(3)}$, $\chi_{xyxy}^{(3)}$, and $\chi_{xyyx}^{(3)}$. $\chi_{xxxx}^{(3)}$ in this case can be expressed as

$$\chi_{xxxx}^{(3)} = \chi_{xxyy}^{(3)} + \chi_{xyxy}^{(3)} + \chi_{xyyx}^{(3)}.$$

Indices x and y here refer to the polarization planes of the interacting beams which propagate along the z-direction. The first and the second indices correspond to the two pump beams which set up the holographic grating. The third and fourth indicate the polarization plane of the incident probe and resulting diffracted beam, respectively. When the polarizations of two pump beams are parallel they interfere to form a sinusoidal intensity, and thus a population grating. In contrast, when the polarizations are perpendicular, interference of the two beams is not possible, and the sample is irradiated with a uniform intensity. Still, a particularly interesting modulation occurs: there will be a polarization grating in which the polarization varies sinusoidally between left and right circular states. In magneto-optically active samples, this obviously leads to a modulation of the magnetization. In other words, a spin grating will be formed with alternating spin-up and spin-down excitations.

In transient grating experiments the laser output was split by a beam splitter into two pulses with a 3:1 intensity ratio (pump and probe, respectively). The pump and probe beams passed through $\lambda/2$-plates, which rotate the plane of polarization, and subsequently through
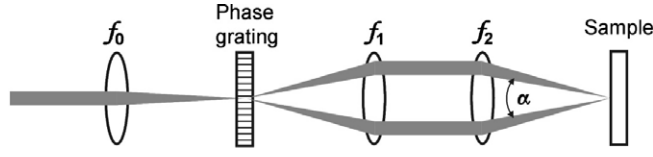
Figure 4. Confocal imaging system used in the transient grating experiments, showing the spatial arrangement of pump beams. The symbols are explained in the main text.

Glan Taylor polarizers to ensure well-defined polarization states. The pump beam then was focused by a $f_0 = 250$ mm focal length lens onto a phase grating with a period of 30 mm^{-1} which is specially designed to diffract about 30% of the input energy into the $+1$ and -1 orders of diffraction. One advantage of using a phase grating is that it produces phase-locked beams, which remain so if the same optical elements are used for them after the grating. In addition, the use of the phase grating ensures optimum spatial overlap of the excitation and probe pulses in the sample [31]. The two pump beams produced by the phase grating were used to write a holographic grating on the sample. The imaging system, based on two lenses with focal length f_1 and f_2 (see figure 4), allows control of the angle between the two writing beams, and so of the holographic grating period Λ:

$$\alpha = 2\arctan\left[\frac{f_1}{f_2}\left(\left(\frac{d}{\lambda}\right)^2 - 1\right)^{-\frac{1}{2}}\right], \qquad \Lambda = \frac{\lambda}{2\sin(\alpha/2)}.$$

Here λ is the wavelength of the irradiation, and d is the spacing of the phase grating. For room-temperature experiments f_1 was 250 mm while f_2 was chosen to be 150 or 80 mm corresponding to grating periods of 11 and 5 μm, respectively (estimated focal spot diameters 45 and 25 μm, respectively). For low-temperature measurements f_2 was replaced by a spherical mirror with a curvature $R = -500$ mm ($f_2 = 250$ mm), corresponding to a grating period of 24 μm (estimated focal spot diameter 75 μm).

The diffracted signal decays as the amplitude of the holographic grating vanishes. The dynamics of the recorded holographic grating were probed by a probe pulse which was delayed with respect to the pump pulses by a computer-controlled delay stage. All three (two pump and a probe) beams were arranged in a so-called BOXCAR geometry. This geometry satisfies phase-matching conditions and allows control over the direction of the diffracted beam. In the BOXCAR arrangement three parallel beams, pump k_1, pump k_2, and probe k_3, are arranged parallel to each other so that they form three corners of a rectangle in a plane perpendicular to their path. A lens (or a focusing mirror) whose centre matches that of this rectangle is used to focus the beams onto the sample. The two pump pulses interfere in the sample and form a population grating from which the third beam diffracts into the direction k_s satisfying the phase-matching conditions, i.e. it emerges through the fourth corner of the rectangle in the direction $k_s = k_3 + k_1 - k_2$. Since the diffracted signal is typically rather weak, the BOXCAR geometry is convenient because the direction of the diffracted beam is strictly determined. During the measurements transient reflectivity (TR) and TG signals were recorded simultaneously by two photodiodes. This allows simultaneous determination of both the photoinduced electron (spin) decay time, and the grating decay time in a single scan. Since transient reflectivity gives information on the population dynamics, and transient grating decay reflects both the spatial diffusion and the population decay, a simultaneous measurement permits separation of these two contributions allowing for a determination of the diffusion coefficient, as detailed in section 3.3.

A basic description of the dynamics of sinusoidal TG formed by photogenerated excess carriers was first developed by Woerdman [32], and reviewed by Eichler *et al* [33]. After

ultrafast holographic excitation excess carriers simultaneously recombine and diffuse within the sample, eventually leading to equilibrium conditions. In the two-dimensional case the interference between the two pump pulses results in a harmonic modulation $\delta N(x, t)$ of the charge density $N(t)$:

$$\delta N(x, t) = \frac{\delta N(t)}{2}(1 + \sin(2\pi x/\Lambda)),$$

where Λ is the period of the grating. When carrier relaxation and diffusion occur on similar timescales, the decay of the grating may be described by [34]

$$\frac{\partial \delta N(x, t)}{\partial t} = D\nabla^2(\delta N(x, t)) - \frac{\delta N(x, t)}{T_r},$$

with T_r the time constant for population relaxation, and D the diffusion coefficient. If the diffusion coefficient does not depend on the space coordinate nor on the charge density then one finds for the population modulation

$$\frac{\partial \delta N(t)}{\partial t} = -\delta N(t)\left[\frac{4\pi^2}{\Lambda^2}D + \frac{1}{T_r}\right],$$

with solution

$$\delta N(t) \propto e^{-\left[\frac{4\pi^2}{\Lambda^2}D + \frac{1}{T_r}\right]t}.$$

Since the diffracted signal is proportional to the square of the population modulation ($I(t) \propto (\delta N(t))^2$) the diffracted signal will decay as

$$I(t) \propto e^{-2[\frac{4\pi^2}{\Lambda^2}D + \frac{1}{T_r}]t}.$$

This leads to the definition of the grating decay rate constant

$$\frac{1}{T_{gr}} = \frac{8\pi^2}{\Lambda^2}D + \frac{2}{T_r},$$

which depends on the grating period Λ, the diffusion coefficient D, and the population decay time constant T_r. The diffusion coefficient and population decay time constant can thus be determined independently from two transient grating experiments using different grating periods. Alternatively, the diffusion constant can also be determined from a simultaneous measurement of the dynamics of the diffracted signal and the population relaxation (time-resolved reflectivity). Once the diffusion coefficient is known, one can calculate the mobility μ using

$$\mu = \frac{eD}{k_b T},$$

where e, k_b, and T are the electron charge, Boltzmann coefficient and the temperature, respectively.

First some results obtained for a heterojunction at room temperature are discussed, which has the advantage that one can easily change the grating period by changing the angle of incidence for the pump beams. Figure 5 shows TR and TG signals measured at room temperature for various probe wavelengths. The pump wavelength was 780 nm with an energy of 1125 pJ/pulse. Evidently, the TR dynamics is wavelength dependent on a sub-100 ps timescale. This might result from a variety of processes such as intraband relaxation, exciton formation, bulk recombination and excited electron migration from the bulk to the heterojunction, as discussed in section 3.2. In contrast, the decay of the TG signal is substantially less probe wavelength dependent. Apparently the fast processes determining the
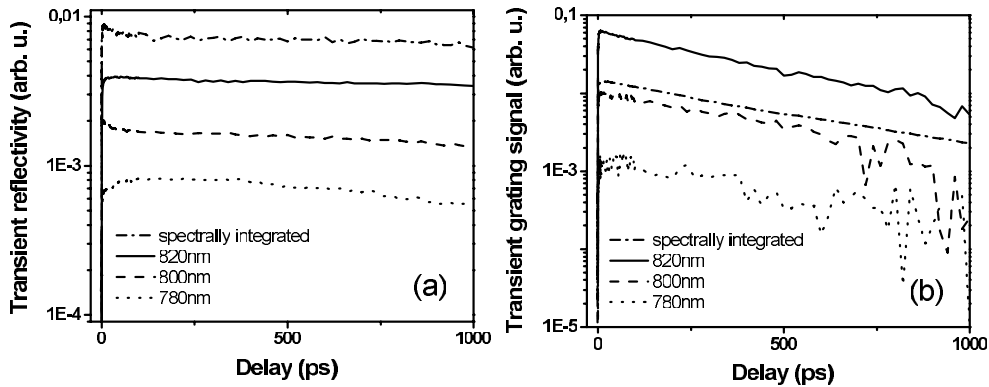
10

Figure 5. The transient reflectivity (a) and transient grating (b) signals measured on the 2DEG sample, at different wavelengths. Data taken at 294 K, no magnetic field, 780 nm pump; probe wavelengths are indicated in the panels.
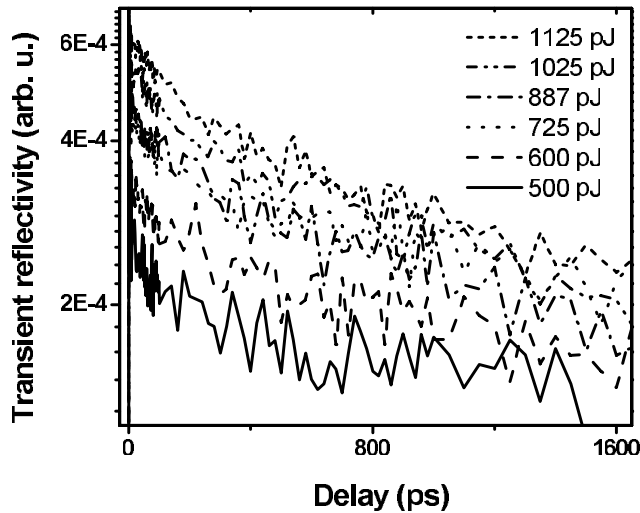

Figure 6. The transient reflectivity measured on the 2DEG sample, at different pump pulse energies. Data taken at 294 K, no magnetic field, 780 nm pump. A fraction of the output of the Ti:sapphire laser was used as probe, without spectral filtering.

initial dynamics of the TR signal do not play a role in the TG dynamics. On the timescale on which the TG signal relaxes, the TR dynamics is practically wavelength independent.

The decay of the TR and TG signals are more strongly dependent on the excitation power, as is shown in figures 6 (TR) and 7 (TG). The TR dynamics evidently speeds up with increasing excitation power, and is well approximated by a two-exponential decay function with typical time constants of about 100 ps and 2 ns. In line with this, the TG decay, measured for grating periods 5 and 11 μm, also becomes faster upon increasing the excitation power (see figure 7). It is nearly single exponential, except for a delayed formation observed during the first tens of picoseconds (see also section 3.2). In order to check for possible accumulation effects such as heating or secondary excitation of long-living photoexcited species, TR and TG measurements were performed at different pulse repetition rates (800 kHz–4 MHz). Since these experiments
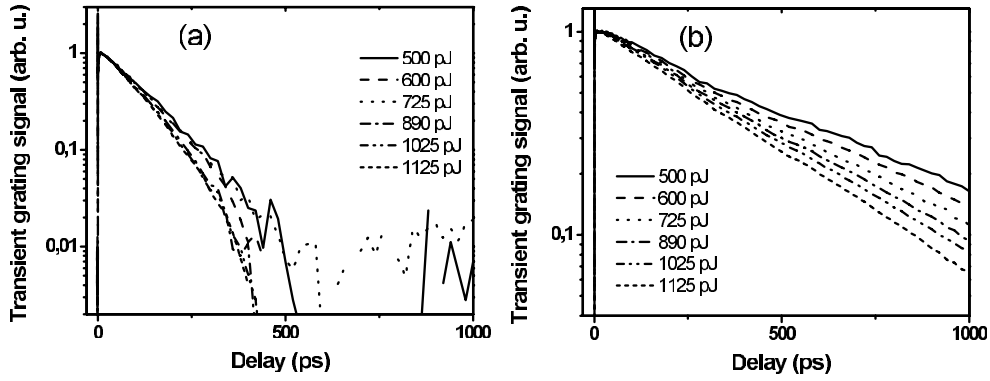
Figure 7. Transient grating decay measured on the 2DEG sample, at different pump pulse energies. The period of gratings is 5 μm (a) and 11 μm (b). Data taken at 294 K, no magnetic field, 780 nm pump. A fraction of the output of the Ti:sapphire laser was used as probe, without spectral filtering.

Table 1. The power-dependent decay time constants of the transient reflectivity signals (T_1^{TR} and T_2^{TR}) and of transient grating signals ($T_{\mathrm{gr}}^{5\,\mu\mathrm{m}}$ for the 5 μm spaced grating, and $T_{\mathrm{gr}}^{11\,\mu\mathrm{m}}$ for the 11 μm spaced grating). Data measured on the 2DEG sample. The last two columns give the population decay constant (T_2^{calc}) and the diffusion coefficient (D) calculated from the two grating time constants. Experimental parameters as in figure 6.

Energy (pJ)	T_1^{TR} (ps)	T_2^{TR} (ns)	$T_{\mathrm{gr}}^{5\,\mu\mathrm{m}}$ (ps)	$T_{\mathrm{gr}}^{11\,\mu\mathrm{m}}$ (ps)	T_2^{calc} (ns)	D (cm^2 s^{-1})
1125	148 ± 28	2.1 ± 0.3	107 ± 1	365 ± 2	2.0	26.4
1025	129 ± 25	2.3 ± 0.4	120 ± 1	369 ± 8	1.6	22.4
887	115 ± 20	2.4 ± 0.3	124 ± 2	389 ± 3	1.8	21.9
725	108 ± 25	3.0 ± 0.9	119 ± 1	438 ± 3	2.9	24.4
600	101 ± 28	3.1 ± 0.9	119 ± 1	478 ± 4	4.5	25.2
500	83 ± 20	3.2 ± 0.7	140 ± 2	523 ± 4	3.6	20.9

showed no dependence of the observed dynamics on the repetition rate one may conclude that heating and secondary excitation processes do not play an important role.

The diffusion coefficient determined from the data of figure 7 is tabulated in table 1. The value of about 25 cm^2 s^{-1}, which is quite independent of the pump power, yields a room-temperature mobility for the photoexcited carriers of $\sim 10^3$ cm^2 V^{-1} s^{-1}. This is almost an order of magnitude smaller than the value determined from room-temperature transport experiments under illumination (8×10^3 cm^2 V^{-1} s^{-1}, which is not surprising since the TG technique is particularly sensitive to the carriers with the lowest mobility. The complicated dynamics of the TR complicates extraction of the diffusion constant from the simultaneous measurements of TR and TG decay, but leads to similar values. Conversely, the population decay constant (T_2^{calc}) extracted from the transient grating experiments with two different grating spacings (5 and 11 μm) is in reasonable agreement with the slow component observed in the TR experiments. The independence of the diffusion constant (the electron mobility) on the excitation density shows that the observed speeding of the decay of the TG signal is solely caused by the faster relaxation of the electron population, as also observed in the transient reflectivity data recorded under the same conditions.

Simultaneous temperature-dependent TR and TG measurements were performed at low temperatures using an $R = -50$ cm spherical mirror instead of the last lens in the imaging
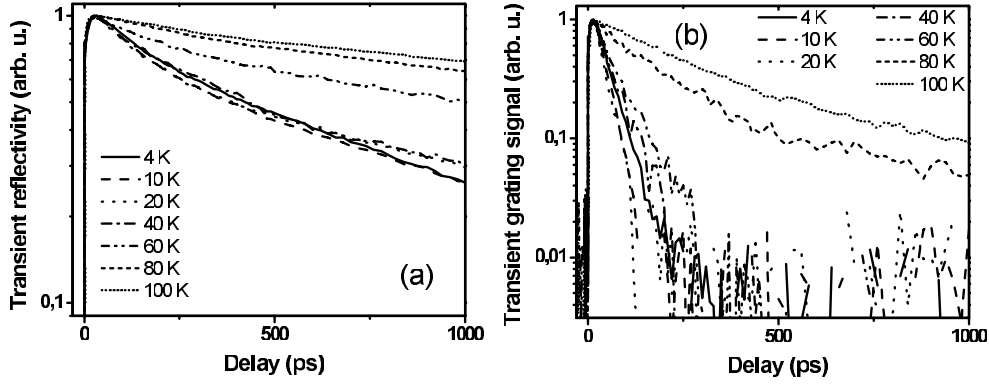
Figure 8. The transient reflectivity (a) and transient grating (b) decay measured on the 2DEG sample, at different temperatures. Data taken with 780 nm pump (pulse energy 1 nJ), and weaker 820 nm probe pulses, no magnetic field.

Table 2. The temperature-dependent decay time constants of the transient reflectivity signal (T^{TR}) and of the transient grating signals ($T_{gr}^{24\,\mu m}$ for a 24 μm spacing grating. The TR decay time constant was evaluated by using a single-exponential approximation in a time window corresponding to the decay of the TG signal. The last two columns give the diffusion coefficient (D) and the mobility (μ) calculated from the TG and TR time constants. Experimental parameters as in figure 8.

Temperature (K)	T^{TR} (ns)	$T_{gr}^{24\,\mu m}$ (ps)	D (cm^2 s^{-1})	μ (cm^2 V^{-1} s^{-1})
294[a]	—	—	26.4	1.0×10^3
100	2.6	230	262	3.0×10^4
80	2.3	149	425	6.2×10^4
60	1.2	67	965	1.9×10^5
40	0.55	53	1111	3.2×10^5
20	0.36	28	2200	1.3×10^6
10	0.4	30	2077	2.4×10^6
4.2	0.58	38	1667	4.8×10^6

[a] Value taken from table 1.

system. This results in a grating period of 24 μm. The wavelength was 780 nm, and the excitation energy was kept at 1125 pJ/pulse throughout the experiments. Some typical TR and TG transients measured at different temperatures are shown in figure 8. The decay of both the TR and (in particular) the TG signals speeds up with decreasing temperature from 100 to 4.2 K. For the TR response this has already been discussed in section 3.2. The faster relaxation of the TG signal at low temperatures reflects a tremendous increase of the mobility at low temperatures, typical for a heterojunction 2DEG. This evidently shows that the measured signal indeed originates from the 2DEG. The mobility as calculated from the decay of the TG and TR signals measured at different temperatures is shown table 2 and figure 9. At 4.2 K the mobility is of the order of 5×10^6 cm^2 V^{-1} s^{-1}, which is comparable to the mobility determined from transport experiments under illumination (2.7×10^6 cm^2 V^{-1} s^{-1}), and substantially larger than the bulk values measured under similar conditions (5×10^4 cm^2 V^{-1} s^{-1}). With increasing temperature the mobility gradually decreases due to the increased scattering rate. It is interesting to note that at temperatures 80 and 100 K the TG response becomes evidently non-single exponential and can be reasonably well approximated by a two-exponential decay function with typical decay constants in the range of 150 ps and a couple of nanoseconds. This
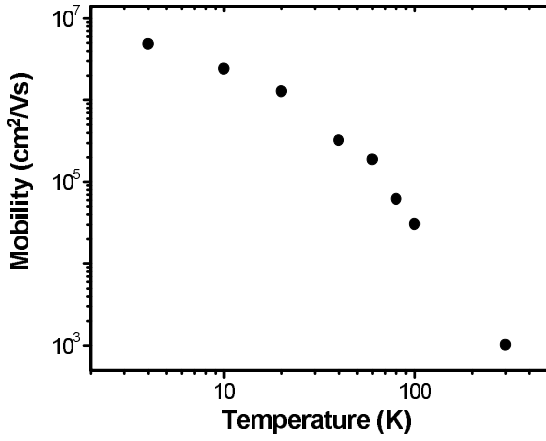
Figure 9. Electron mobility of a 2DEG as a function of temperature, as derived from transient grating data as in figure 8.

probably results from the presence of two charge-carrier species, one in the 2DEG, and one in the buffer layer, each with their own temperature-dependent response originating from the temperature dependence of the band gap.

4. Spin dynamics

4.1. Transient magneto-optics: TRKR

Electron spin dynamics was investigated in the heterojunction structures by time-resolved Kerr rotation (TRKR). This technique is sensitive to the evolution of spin-polarized carriers on ultra-short timescales. A circularly polarized pump pulse first promotes an unequal number of spin-up and spin-down electrons to the conduction band of the semiconductor. Subsequently, a linearly polarized probe pulse is reflected from the sample. By analysing the change in polarization state of the probe beam, the magnetization of the sample along the direction of the probe beam can be traced at a given instant [35]. A TRKR trace is obtained by scanning the delay between the pump and probe pulses using a mechanical delay line.

The TRKR set-up is similar to the one used for the transient reflectivity measurements, with appropriate changes for controlling the polarization state of both the pump and probe pulses. To improve the signal to noise ratio, a lock-in technique is used with a photo-elastic modulator that modulates the polarization of the pump beam between right and left circular polarizations at a rate of 50 kHz. The rotations of the plane of polarization of the probe pulses, corresponding to the Kerr rotation angle, are detected using a balanced photodiode bridge. A schematic diagram of the beam geometry utilized is depicted in figure 10.

In the presence of an in-plane external magnetic field, the spins injected by the pump pulse precess at the Larmor frequency Ω_L given by

$$\vec{\Omega}_L = g\mu_B \vec{B}/\hbar \tag{1}$$

where g is the electron g-factor, μ_B is Bohr's magneton, B is the applied magnetic field and $\hbar$ is the reduced Planck constant. Spin precession shows up in TRKR traces as distinct oscillations of the Kerr angle. Figure 11 shows low-temperature TRKR traces taken on a sample of bulk n-type GaAs (figures 11(a) and (b)) at 7 and 0 T respectively. The doping concentration of the bulk sample (3×10^{16} cm^{-3} Si doping) was chosen equal to a well-characterized material, that was reported to give the longest spin coherence times in bulk GaAs [4]. The electron g-factor can be determined from the measured precession frequency at $B \neq 0$ utilizing equation (1). The g-factor in turn gives important information about the optically pumped spin population.
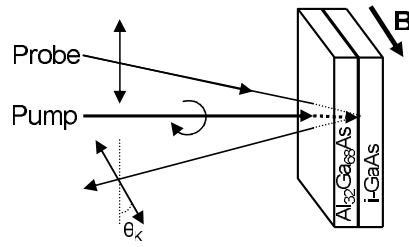
Figure 10. Schematic diagram of the pump and probe beams incident on the 2DEG sample as used in TRKR experiments. The pump pulse is circularly polarized and the probe is linearly polarized. The pulses are incident on the sample at a small angle from the normal ($\sim$2.3°). Time traces are taken by scanning the delay between the pump and probe pulses. A rotation of the probe pulse polarization (θ_K) is induced by the instantaneous alignment of spins in the conduction band of the semiconductor. The applied magnetic field is oriented in the plane of the 2DEG.
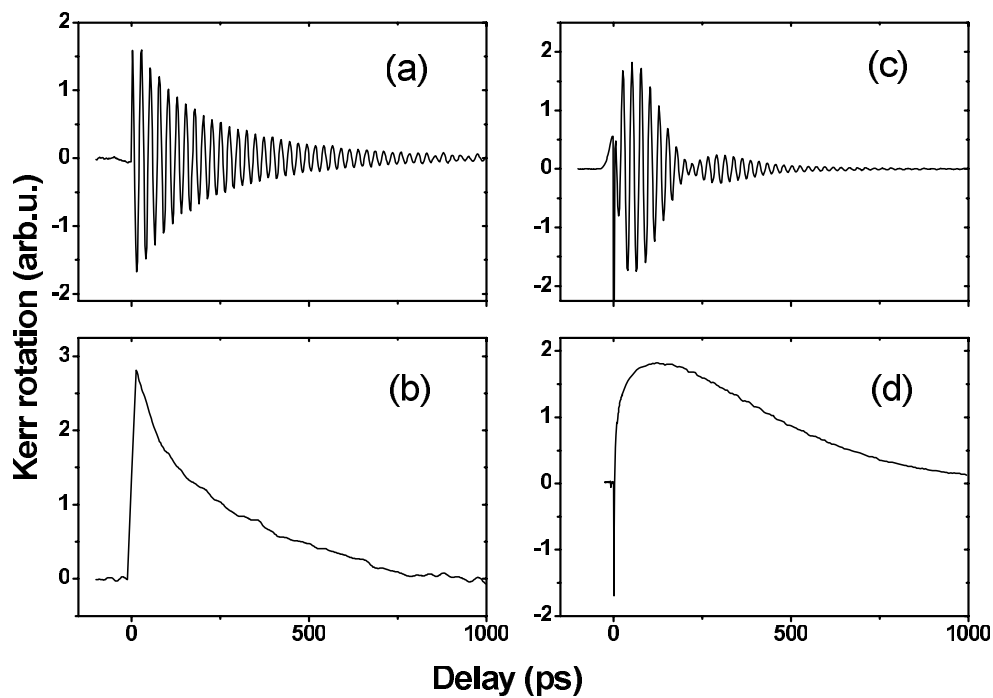

Figure 11. Time-resolved Kerr rotation signal at 4.2 K from bulk n-GaAs at 7 T (a) and 0 T (b) and from the heterojunction 2DEG also at 7 T (c) and 0 T (d). The data show considerable differences between the spin dynamics in bulk and 2DEG samples. Most remarkable is the presence of beatings in the signal taken at 7 T in the 2DEG sample (plot (c)). Also in the 2DEG, comparing plots (b) and (d) clearly shows a slow increase of the Kerr signal in the delay range 0–100 ps. Data taken with 780 nm pump (0.8 nJ/pulse), and weaker 820 nm probe pulses.

For bulk GaAs a g-factor of $|g| \sim 0.44$ is found, consistent with the accepted value for this material of $g \simeq -0.44$. The loss of coherence of the photoexcited spins can be studied by measuring TRKR traces at $B = 0$ or the envelopes of the oscillatory signal at $B \neq 0$.

The traces taken on n-GaAs should be compared to the ones taken on the heterojunction structure under similar conditions, figures 11(c) and (d). In the HJ2DEG traces clear beatings are seen in the data taken at 7 T, providing evidence of the existence of two spin populations

15

with different g-factors. The g-factors determined from the data in figure 11(c) are $|g| \sim 0.44$ and $|g| \sim 0.39$. These values suggest the existence of both a 3D ($|g| \sim 0.44$) and a 2D ($|g| \sim 0.39$) [36] spin (and charge) population.

The TRKR traces for the HJ2DEG sample, figures 11(c) and (d), show a slow increase of the Kerr rotation angle amplitude, reaching a maximum at approximately 100 ps. The origin of this signal increase is analogous to the origin of the increase in the transient reflectivity signal as discussed in the previous section. Again it is needed that the two distinct carrier populations give Kerr rotations of opposite signs, which again may easily arise from the spectral details in the Kerr response. Assuming two different spin populations with different dephasing times and different g-factors gives a satisfactory description of the observed data.

5. Combined spin and charge dynamics: MEOKE

5.1. Experimental techniques for EOKE and MEOKE

To introduce MEOKE, it is useful to first describe the electro-optical Kerr effect (EOKE). The EOKE is the rotation of the plane of polarization of an optical probe field in an external electric field. Excitation of a material by an ultra-short laser pulse induces a transient anisotropy of the refractive index, resulting in a rotation of polarization and an induced ellipticity of a subsequent probe pulse reflected off the excited material. The photoinduced anisotropy vanishes as photoinduced excitations lose their orientational memory or relax to the ground state. From a magneto-optical point of view, EOKE can be viewed as an excitation of σ^+ and σ^- transitions leading to two populations that are coherent with the excitation. In zero magnetic field these populations are degenerate, resulting in a non-spin-polarized macroscopic dielectric polarization P [37], which in turn leads to the photoinduced anisotropy. In the presence of an external magnetic field B, the Zeeman splitting of the energy levels ($\Delta E = g\mu_B B$) removes the degeneracy of the states populated by the σ^+ and σ^- transitions. This leads to a macroscopic polarization P which is now determined by a coherent superposition of the energy-split states. The superposition oscillates at the Larmor frequency $\omega = \Delta E/\hbar$ resulting in a rotation of the polarization around the direction of B. The rotation of P around the magnetic field results in a modulation of the polarization of the reflected probe beam, similar to that in the TRKR experiments. The strength of the modulation depends on the angle at which the probe field propagates with respect to the direction of the external magnetic field B. Again, as for TRKR, for zero degrees incidence the modulation will be maximal. In general the response will reflect both the decay of the coherence of the induced population and the dephasing of the spin precession.

In the electro-optical Kerr effect (EOKE) experiments the sample was excited with linearly polarized light while photoinduced anisotropy was recorded by analysing the polarization changes of a reflected weak probe beam which is initially polarized at $45°$ with respect to the pump. The sample's normal was oriented at an angle of $\sim 5°$ with respect to the propagation direction of the probe beam. For EOKE experiments in an external magnetic field (MEOKE), this results in a nearly transverse geometry when the applied magnetic field is practically perpendicular to the **k**-vector of the excitation and probe light, and is parallel to the 2DEG plane of the HJ2DEG sample.

5.2. MEOKE results

Figure 12 shows transient birefringence decay curves at 4 K for two different applied magnetic fields. The pump energy is 250 pJ; excitation and probe were centred at 780 and 820 nm respectively. The time evolution of the signal can be described as a decay modulated by oscillations. Again, an initial growth is observed, similar to the growth seen in the other
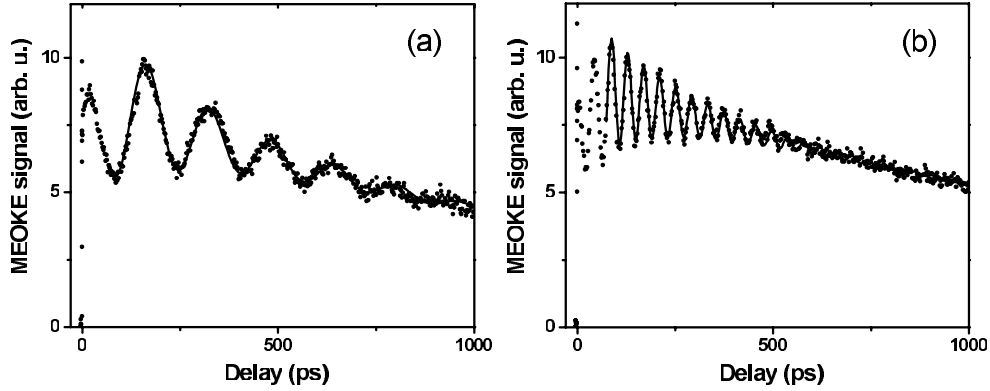
Figure 12. MEOKE signals at 4.2 K for 1 T (a) and 4 T (b) applied magnetic fields, measured on the 2DEG sample. Dots are experimental data, solid lines are fits. Data taken with 780 nm pump (250 pJ/pulse), and weaker 820 nm probe pulses.

Table 3. Electron and spin life time, and precession frequency at different magnetic fields from MEOKE experiments on the 2DEG sample. Data taken at 4.2 K, 780 nm pump (250 pJ/pulse), and weaker 820 nm probe pulses.

Field (T)	T_e (ps)	T_s (ps)	ω (GHz)
1	1518 ± 20	351 ± 7	6.35
2	1487 ± 15	268 ± 5	11.8
4	1444 ± 25	210 ± 9	23.8
7	1421 ± 14	205 ± 3	42.3

Table 4. Electron and spin decay times for different excitation pulse energies, from MEOKE experiments on the 2DEG sample. The measurements were performed with 780 nm pump and 820 nm probe pulses at temperature of 4.2 K in an external magnetic field of 7 T.

Energy (pJ)	T_e (ps)	T_s (ps)
100	1815	504
250	1481	286
437	1221	210
877	1040	118
1500	875	60

experiments. It is evident that the amplitude of the oscillations decays substantially faster than the population decay, indicating that the spin dephasing occurs on a shorter timescale than the loss of induced charge coherence. Consequently, MEOKE experiments potentially allow simultaneous tracing of the dynamics of both spin and charge coherence. The measured traces (neglecting the initial growth) were fitted using

$$I(t) = A_1 e^{-t/T_e} + A_2 e^{-t/T_s} \sin(\omega t + \phi),$$

with T_e the decay time constant of photoinduced anisotropy, T_s the spin dephasing time, and ω the precession frequency. The time constants and the precession frequency for different strengths of applied external magnetic field at a temperature of 4 K are given in table 3. The *g*-factor deduced from these experiments is slightly dependent on the excitation density and amounts to −0.43 and −0.42 for the excitation pulse energies of 100 pJ and 1.5 nJ respectively (see figure 13).
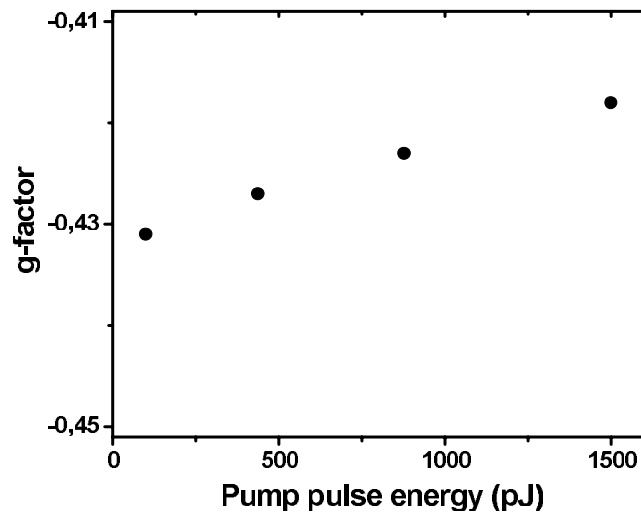
17

Figure 13. The *g*-factor derived from MEOKE measurements as a function of pump pulse energy for the 2DEG sample, derived from data as in figure 12. The measurements were performed with 780 nm pump and 820 nm probe pulses at a temperature of 4.2 K in an external magnetic field of 7 T.
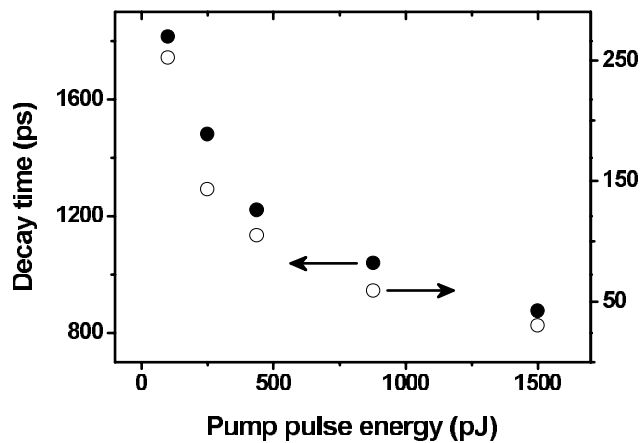

Figure 14. Electron (solid circles) and spin (open circles) decay times at different pump pulse energies for the 2DEG sample, derived from data as in figure 12. The measurements were performed with 780 nm pump and 820 nm probe pulses at a temperature of 4.2 K in an external magnetic field of 7 T.

MEOKE experiments at different excitation densities reveal a strong dependence of the dynamics of both charges and spins on the excitation pulse energy, as is the case in TR and TRKR experiments. Furthermore, the results reveal that the spin dephasing time decreases much faster than the charge phase memory upon increasing excitation energy. Although the nature of this behaviour is still unclear, it does show that the internal relaxation between spin-split levels strongly depends on scattering processes between electrons in highly excited states. Finally note that the value of the *g*-factor is slightly power dependent, resulting from the increasing average energy of the photoinduced charge carriers. The results for several excitation powers are summarized in figure 13 for the *g*-factor, and in table 4 and figure 14.

6. Summary and conclusions

Optical experiments on the charge and spin dynamics in a heterojunction structure show a quite complex behaviour. The high-mobility 2DEG does have characteristic features in, for instance, the photoluminescence, the transient reflectivity, and the time-resolved Kerr rotation, but these have to be discriminated from the features originating from in particular the 3D buffer layer. The interpretation of the observed phenomena is further complicated by the changes in the HJ2DEG potential resulting from the photoinduced charges. Nevertheless, important information can be extracted from the optical experiments. The photoluminescence evidences, for instance, the existence of indirect 2D electron–3D hole exciton recombination resulting from interaction of the 2DEG charges with acceptor-bound holes in the surrounding bulk. The transient magneto-optical Kerr rotation experiments showed the existence of two populations of photoexcited charge carriers. It appears from the time-resolved reflectivity experiments that each of them has its own relaxation time and they contribute to the observed transient reflectivity with different signs at 820 nm probe wavelength. The size, sign and decay times of the contributions of the different populations depend strongly not only on the probe wavelength but also on the excitation power. This originates from the details of the electronic structure for the 2D and 3D electrons, from carrier diffusion, and from optically induced band-bending and renormalization effects. One of the best methods to study the charge dynamics is the transient grating technique, since it allows one to discriminate between population decay dynamics and diffusion processes. As a bonus one also obtains the mobility of the charge carriers. A variant of this technique, using a polarization grating rather than an intensity grating, has also proved to be quite successful in the study of spin dynamics [29, 30]. The most straightforward technique to study the spin dynamics is the time-resolved Kerr rotation experiment. The two species of charge carriers probed in these experiments led to a beating of the precession oscillations in the TRKR traces. These TRKR experiments also show that the dephasing time of the spin population can be much faster than the charge population decay (270 ps and 1.2 ns, respectively measured at 4.2 K and 0 T with 780 nm pump of 0.8 nJ per pulse and 820 nm probe light). Most likely, this relatively fast dephasing results from the high mobility of the 2DEG in combination with the D'yakonov–Perel' mechanism [38], in which the spin population of an ensemble of electrons propagating in different directions dephases due to the anisotropy of the spin–orbit field. This difference in spin dephasing and charge decay times is also found in a simultaneous measurement of the charge and spin dynamics using the magneto-electro-optical Kerr effect. Again the dephasing time is found to be quite a bit faster than the charge decay. Moreover, the spin dephasing time rapidly decreases upon increasing excitation power. Whereas for moderate powers (100 pJ) this time is about half a nanosecond, it is only 60 ps at high power (1500 pJ). The origin of this rapid quenching of the spin lifetime is not quite clear at present; possibly it results from a larger *g*-factor spread at high excitation density or maybe even from enhanced spin-flip momentum scattering through the Elliot–Yafet mechanism [39, 40].

Acknowledgments

References

[1] Wolf S A, Awschalom D D, Buhrman R A, Daughton J M, von Molnár S, Roukes M L, Chtchelkanova A Y and Treger D M 2001 *Science* **294** 1488 and references therein

[2] Žutić I, Fabian J and Das Sarma S 2004 *Rev. Mod. Phys.* **76** 323 and references therein
[3] Schmidt G 2005 *J. Phys. D: Appl. Phys.* **38** R107 and references therein
[4] Kikkawa J M and Awschalom D D 1998 *Phys. Rev. Lett.* **80** 4313
[5] Kikkawa J M and Awschalom D D 1999 *Nature* **397** 139
[6] Kikkawa J M, Gupta J A, Malajovich I and Awschalom D D 2001 *Physica* E **9** 194
[7] Kikkawa J M, Smorchkova I P, Samarth N and Awschalom D D 1997 *Science* **277** 1284
[8] Holleitner A W, Sih V, Myers R C, Gossard A C and Awschalom D D 2006 *Phys. Rev. Lett.* **97** 036805
[9] Hanson R, Witkamp B, Vandersypen L M K, Willems van Beveren L H, Elzerman J M and
      Kouwenhoven L P 2003 *Phys. Rev. Lett.* **91** 196802
[10] Kukushkin I and Timofeev V 1996 *Adv. Phys.* **45** 147
[11] Störmer H L, Dingle R, Gossard A C, Wiegmann W and Sturge M D 1979 *Solid State Commun.* **29** 705
[12] Shen J X, Oka Y, Hu C Y, Ossau W, Landwehr G, Friedland K J, Hey R, Ploog K and Weimann G 1999 *Phys. Rev.* B **59** 8093
[13] Miller D A B, Chemla D S, Damen T C, Gossard A C, Wiegmann W, Wood T H and Burrus C A 1984 *Phys. Rev. Lett.* **53** 2173
[14] Yuan Y R, Pudensi M A A, Vawter G A and Merz J L 1985 *J. Appl. Phys.* **58** 397
[15] Zhao Q X, Bergman J P, Holtz P O, Monemar B, Hallin C, Sundaram M, Merz J L and Gossard A C 1990 *Semicond. Sci. Technol.* **5** 884
[16] Kim D Y, Kang T W and Kim T W 1995 *Thin Solid Films* **261** 168
[17] Zhao Q X, Bergman J P, Holtz P O, Monemar B, Ensslin K, Sundaram M, Merz J L and Gossard A C 1991 *Superlatt. Microstruct.* **9** 161
[18] Yang C H, Lyon S A and Tu C W 1988 *Appl. Phys. Lett.* **53** 285
[19] Kukushkin I V, von Klitzing K and Ploog K 1988 *Phys. Rev.* B **37** 8509
[20] Turberfield A J, Haynes S R, Wright P A, Ford R A, Clark R G, Ryan J F, Harris J J and Foxon C T 1990 *Phys. Rev. Lett.* **65** 637
[21] Buhmann H, Joss W, von Klitzing K, Kukushkin I V, Martinez G, Plaut A S, Ploog K and Timofeev V B 1990 *Phys. Rev. Lett.* **65** 1056
[22] Chaves A S, Penna A F S, Worlock J M, Weimann G and Schlapp W 1986 *Surf. Sci.* **170** 618
[23] Chou M J, Tsui D C and Weimann G 1985 *Appl. Phys. Lett.* **47** 609
[24] Bergman J P, Zhao Q X, Holtz P O, Monemar B, Sundaram M, Merz J L and Gossard A C 1991 *Phys. Rev.* B **43** 4771
[25] Prabhu S S and Vengurlekar A S 2004 *J. Appl. Phys.* **95** 7803
[26] Alexandrou A, Berger V and Hulin D 1995 *Phys. Rev.* B **52** 4654
[27] Leo K, Rühle W W and Ploog K 1988 *Phys. Rev.* B **38** 1947
[28] Gurioli M, Vinattieri A, Colocci M, Deparis C, Massies J, Neu G, Bosacchi A and Franchi S 1991 *Phys. Rev.* B **44** 3115
[29] Weber C P, Gedik N, Moore J E, Orenstein J, Stephens J and Awschalom D D 2005 *Nature* **437** 1330
[30] Carter S G, Chen Z and Cundiff S T 2006 *Phys. Rev. Lett.* **97** 136602
[31] Maznev A A, Crimmins T F and Nelson K A 1998 *Opt. Lett.* **23** 1378
[32] Woerdman J P 1971 *Philips Res. Rep. Suppl.* **7** 65
[33] Eichler H, Gunther P and Pohl D 1986 *Laser Induced Dynamic Gratings* (Berlin: Springer)
[34] Moss S C, Lindle J R, Mackey H J and Smirl A L 1981 *Appl. Phys. Lett.* **39** 227
[35] Meier F and Zakharchenya B P 1984 *Optical Orientation* (Amsterdam: North-Holland)
[36] Hannak R M, Oestreich M, Heberle A P, Rühle W W and Köhler K 1995 *Solid State Commun.* **93** 313
[37] Worsley R E, Traynor N J, Grevatt T and Harley R T 1996 *Phys. Rev. Lett.* **76** 3224
[38] D'yakonov M I and Perel' V I 1972 *Sov. Phys.—Solid State* **13** 3023
[39] Elliot R J 1954 *Phys. Rev.* **96** 266
[40] Yafet Y 1963 *Solid State Phys.* vol 14, ed F Seitz and D Turnbull (New York: Academic) pp 1–98